Rapid Communications

Superconductivity in the nonsymmorphic line-nodal compound CaSb$_2$

Atsutoshi Ikeda [ORCID],[1,*] Mayo Kawaguchi,[1] Shun Koibuchi,[1] Tatsuki Hashimoto,[2] Takuto Kawakami,[3]
Shingo Yonezawa [ORCID],[1] Masatoshi Sato,[2] and Yoshiteru Maeno[1]

[1]*Department of Physics, Kyoto University, Kyoto 606-8502, Japan*
[2]*Yukawa Institute for Theoretical Physics, Kyoto University, Kyoto 606-8502, Japan*
[3]*Department of Physics, Osaka University, Toyonaka 560-0043, Japan*

We found superconductivity in CaSb$_2$ with the transition temperature of 1.7 K by means of electrical-resistivity, magnetic-susceptibility, and specific-heat measurements. This material crystallizes in a nonsymmorphic structure and is predicted to have multiple Dirac nodal lines in the bulk electronic band structure protected by symmetry even in the presence of spin-orbit coupling. We discuss a possible topological superconductivity for the quasi-two-dimensional band originating mainly from one of the antimony sites.

I. INTRODUCTION

Topological quantum phenomena have been one of the hottest topics in recent condensed-matter physics [1–3]. Many fascinating topological phenomena such as the surface Dirac cone and spin current have been actively investigated in topological insulators. Moreover, superconductors are also classified by topology [4–6]. Topological superconductors are intimately related to topological insulators, and indeed topological superconductivity was found in a doped topological insulator [7–10].

Nowadays, Dirac and Weyl semimetals have been attracting much attention as new kinds of topological materials [11,12]. These materials are characterized by the topologically or symmetrically protected gapless point in the bulk electronic states in the reciprocal space. Such gapless points lead to peculiar properties such as ultrahigh mobility, chiral anomaly, and surface Fermi arcs. It is also predicted that Dirac and Weyl semimetals can become topological superconductors [13–15]. Thus, superconductivity experimentally found in pressurized and doped Dirac materials [16,17] can be leading candidate for realization of topological superconductors.

More recently, the concept of the Dirac and Weyl semimetals has been extended to the line-nodal materials, in which the bulk energy gap closes along a line in the Brillouin zone [18–20]. These materials are predicted to exhibit several notable phenomena including a long-ranged Coulomb interaction [21], a large surface polarization charge [22], and quasitopological electromagnetic response [23]. Furthermore, if superconductivity is induced in the materials with torus-shaped Fermi surfaces derived from nodal loops, topological crystalline and second-order topological superconductivity is expected to be realized [24].

Although many materials can have nodal lines originating from band crossings in the absence of spin-orbit coupling, such nodal lines generally become gapped in the presence of spin-orbit coupling and the material turns into an insulator or a point-nodal semimetal [19,25]. An additional symmetry such as nonsymmorphic (screw or glide) symmetry is necessary to retain the gapless nodal lines [18]. Thus, so far, only a limited number of materials are proposed as line-nodal materials in the presence of spin-orbit coupling [26–29], and superconductivity in materials with such nodal lines robust against spin-orbit interaction is even more limited [30].

In this paper, we report discovery of superconductivity with the transition temperature $T_c = 1.7$ K in the nonsymmorphic metal CaSb$_2$. A band-structure calculation shows that CaSb$_2$ has several nodal lines protected by the screw and mirror symmetries of the space group $P2_1/m$ even in the presence of spin-orbit coupling and that some nodes cross the Fermi energy [31]. We present evidence of bulk superconductivity obtained by means of magnetic susceptibility, resistivity, and specific heat. The zero-temperature upper critical field is found to be around 0.2 T, corresponding to the coherence length of 40 nm. We also discuss the possibility of topological superconductivity. This superconductivity in a nonsymmorphic nodal-line material can trigger exploration of possible novel superconducting phenomena originating from the robust nodal lines.

II. EXPERIMENT

Stoichiometric mixture of Ca (Sigma-Aldrich, 99.99%) and Sb (Rare Metallic, 99.99%) was placed in an alumina crucible (IRIE Corporation, SSA-S), and the crucible was sealed in a quartz tube under 0.2 atm of argon at room temperature. The tube was heated up to 1000 °C in 3 h, kept at that temperature for 24 h using a box furnace (Denken,
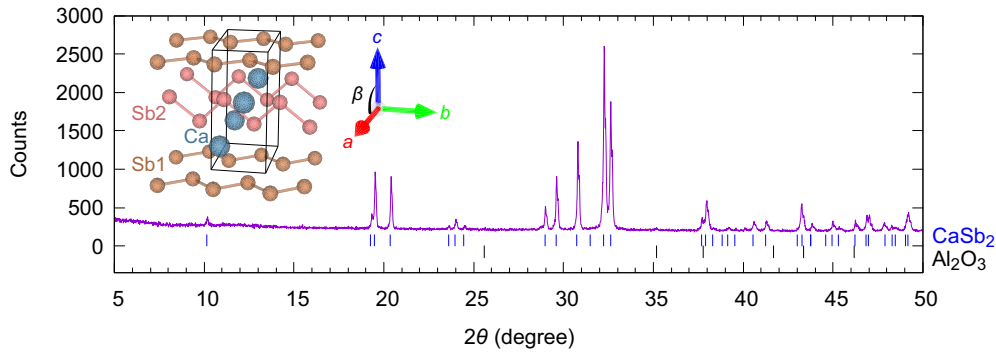

FIG. 1. Powder x-ray diffraction pattern of a CaSb$_2$ sample. The lattice parameters of CaSb$_2$ were extracted to be $a = 0.4741$ nm, $b = 0.4182$ nm, $c = 0.9073$ nm, and $\beta = 106.3°$, in agreement with the previous studies [31,32]. The bars at the bottom indicate the reported peak positions of CaSb$_2$ (blue bars; PDF 01-071-0135) and Al$_2$O$_3$ (black bars; PDF 01-089-7716). For our sample, very small peaks of the latter are attributable to a contamination from crucibles. The inset shows the crystalline structure of CaSb$_2$ with the nonsymmorphic space group $P2_1/m$ (No. 11, C_{2h}^2) with the screw axis along b. The structural image is produced using the program VESTA [33].

KDF 80S), and quenched in water in order to prevent the phase splitting into Ca$_{11}$Sb$_{10}$ and Sb [34]. The sample was then ground and pelletized in an argon atmosphere. The pellet was sealed again in a quartz tube under 0.3 atm of argon at room temperature. The tube was heated to 550 °C in 2 h, kept for 48 h, and furnace cooled. Subsequent measurements are all performed using pelletized polycrystalline samples. This second annealing temperature was chosen to be below the CaSb$_2$-Sb eutectic temperature of 587 °C [34]. We also tried a method similar to the previously reported one, starting from a molar ratio of Ca:Sb = 1:3.9 [31] and slow cooling from 700 °C to 570 °C, but it resulted in a sample containing more additional Sb side product.

Powder x-ray diffraction (PXRD) was measured with a commercial diffractometer equipped with an array of 192 detectors (Bruker AXS, D8 Advance) using the Cu-$K\alpha$ radiation. We did not find any trace of decomposition of CaSb$_2$ even after the sample was kept in air at room temperature for more than two weeks.

Direct-current (DC) magnetization was measured with a commercial magnetometer using a superconducting quantum interference device (Quantum Design, MPMS-XL) equipped with a ^{3}He refrigerator (IQUANTUM, iHelium3). A cut pellet of 50.6 mg (approximately 3.3 × 3.4 × 1.0 mm^3) was used. Alternating-current (AC) magnetic susceptibility was measured with a lock-in amplifier (Stanford Research Systems, SR830) using a miniature susceptometer [35] compatible with an adiabatic demagnetization refrigerator (ADR) of a commercial apparatus (Quantum Design, PPMS).

The electrical resistivity was measured by a standard four-probe method using the ADR option of PPMS. Gold wires with a diameter of 25 μm were attached to a cut pellet using room-temperature-cure silver paste (DuPont Electronics Material, 4929N) with n-butyl acetate as solvent. We comment that zero resistance was not observed when we used silver epoxy (Epoxy Technology, H20E), possibly because the sample reacted with air or with the silver epoxy during the curing process at 120 °C.

Heat capacity from 0.42 to 3.4 K was measured using a calorimeter for a ^{3}He option of PPMS, by using the relaxation method. A cut pellet of 15.7 mg (approximately

2 × 2 × 1 mm^3) was fixed on the sample stage with a thin layer of grease (Apiezon, N-grease) to obtain good thermal connection. For each measurement, a heat pulse raised the sample temperature by 3% of the bath temperature and the temperature relaxation curve was fitted using a double exponential function to evaluate the heat capacity.

III. RESULTS

First, we present the PXRD pattern in Fig. 1. The pattern revealed that our CaSb$_2$ sample is single phased, except for a slight Al$_2$O$_3$ impurity attributable to contamination from the crucible. The lattice parameters of the CaSb$_2$ phase were extracted to be $a = 0.4741$ nm, $b = 0.4182$ nm, $c = 0.9073$ nm, and $\beta = 106.3°$ with the space group $P2_1/m$ (No. 11, C_{2h}^2) by the Rietveld analysis with a weighted pattern R value $R_{wp} = 12.7\%$ and goodness of fit $S = 1.21$. The fitting errors were about 0.002%. These lattice parameters are consistent with the previous reports within 0.06% [31,32].

Next, we show the DC magnetic susceptibility in Fig. 2. Strong diamagnetism indicates superconductivity below 1.8 K. The susceptibility reaches -1.54 at 0.5 K under 0.5 mT. Assuming a rectangular sample shape, the superconducting shielding fraction after demagnetization correction is estimated to be 79% [36]. Later in this paper, the volume fraction is evaluated from the specific heat to be 65%. The susceptibility is suppressed to -0.33 under 5 mT, suggesting a lower critical field H_{c1} smaller than 5 mT.

Figure 3 shows the AC susceptibility of CaSb$_2$. Diamagnetism in the real part of the susceptibility, as well as a small peak in the imaginary part, was observed with an onset of 1.7 K, with an AC field of 3.3 or 8.2 μT. In addition to the transition at 1.7 K, we observed another broad feature at around 1 K signaled by an additional increase in the diamagnetic signal and by a large and broad peak in the imaginary part. For the following three reasons, we consider that this second feature reflects the percolation of the superconducting current among the polycrystalline grains. Firstly, the shielding fraction changes with the amplitude of the AC field only below the second anomaly as shown in Fig. 3. Secondly, the second feature is absent in the DC magnetic susceptibility as
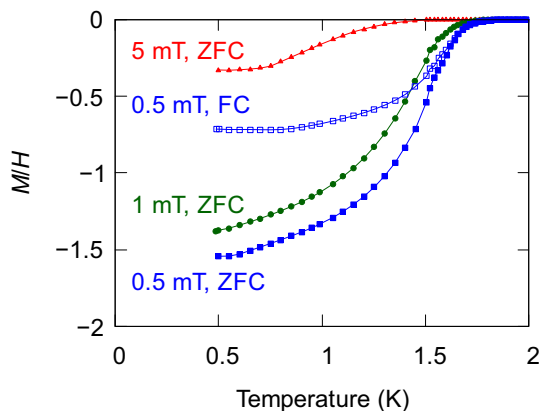
FIG. 2. Temperature dependence of the volumetric DC magnetic susceptibility of $CaSb_2$, measured under various fields with zero-field-cooled (ZFC) or field-cooled (FC) conditions. The Meissner effect with the onset of 1.8 K was observed. The shielding fraction after demagnetization correction reaches 79% at 0.5 K under 0.5 mT with the ZFC process.
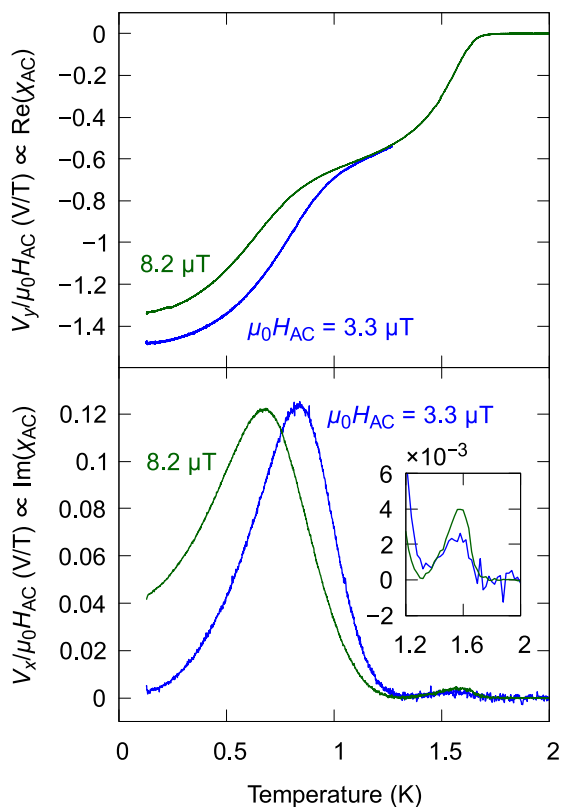

FIG. 3. Temperature dependence of voltage signals detected by the mutual inductance coil normalized by the AC-field amplitude $\mu_0 H_{AC}$. The out-of-phase signal V_y and the in-phase signal V_x are proportional to the real and imaginary parts of the AC susceptibility of $CaSb_2$, respectively. These data were obtained under the AC fields with a frequency of 3011 Hz and amplitudes of 3.3 and 8.2 μT. The Meissner effect was observed below 1.7 K. As seen in the inset of the bottom panel, a small peak in the imaginary part was observed. The feature at around 1 K originates from percolation of the superconducting current between polycrystalline grains (see text).
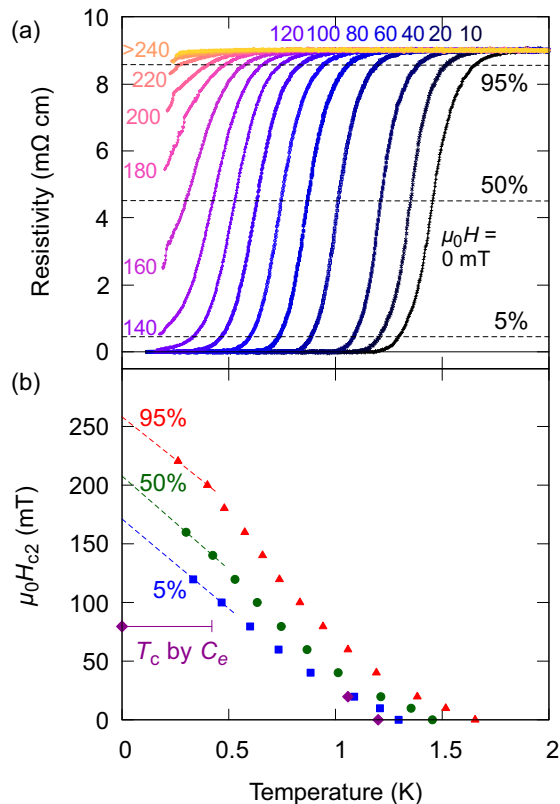

FIG. 4. (a) Temperature dependence of the resistivity of $CaSb_2$ measured under 0 mT, 10 mT, and 20 to 280 mT with an interval of 20 mT. Zero resistance was observed below 1.2 K under zero field. The dashed horizontal lines present 5, 50, and 95% of the normal-state value. (b) Superconducting phase diagram deduced from the resistivity data. The transition temperature under each field was defined as the temperature at which the resistivity becomes 5, 50, and 95% of that in the normal state. The dashed lines present the result of the linear fitting to the transition temperatures of each definition. The upper critical field $\mu_0 H_{c2}$ at 0 K was estimated to be 0.17–0.26 T. Also plotted are the thermodynamic T_c evaluated from the specific heat discussed later.

shown in Fig. 2. Thirdly, the peak of the imaginary part of the AC susceptibility is about 40 times larger at 1 K than at 1.6 K under 3.3 μT, even though the diamagnetism seen in the real part is comparable. These behaviors cannot be explained by the bulk effect and are consistent with the Josephson coupling across the grain boundary. The shielding fraction decreases with increasing AC field because the induced supercurrent exceeds the critical current of the grain boundary. In addition, there is a large energy dissipation due to rapid movement of vortices along the boundary. Similar grain-boundary effect has been reported in various polycrystalline or inhomogeneous materials [37,38].

The temperature dependence of the resistivity is presented in Fig. 4(a). Under cooling at zero field, the resistivity starts to decrease at 1.8 K and reaches zero at 1.2 K. The large resistivity value of 9 mΩ cm in the normal state is probably dominated by scatterings at the grain boundaries. The superconductivity is suppressed as we apply the magnetic field, and above 120 mT the zero resistivity was not observed down to

0.16 K. Figure 4(b) shows the superconducting phase diagram deduced from the field dependence of the resistivity. The transition temperature at each field was defined as the temperature at which the resistivity becomes 5, 50, and 95% of the normal-state value. As we can see especially in T_c determined by the 95% criteria, the slope of the phase boundary becomes steeper above 40 mT. This behavior might be related to the second feature observed in the AC susceptibility (Fig. 3). Small applied magnetic field may break the superconductivity at the grain boundary. As a result, the resistance increases and consequently the transition temperature rapidly decreases with small field. At relatively low temperature, or in the high-field region in the phase diagram, superconductivity at the grain boundary seems less sensitive to magnetic field. Due to this enhancement, we adopted a linear extrapolation of the upper critical field at the low temperatures instead of the ordinary Werthamer-Helfand-Hohenberg relation. Then the upper critical field $\mu_0 H_{c2}$ at 0 K is estimated to be 0.17–0.26 T depending on the definition of T_c. These values correspond to the Ginzburg-Landau coherence length of $\xi_{GL} = \sqrt{\Phi_0/(2\pi\mu_0 H_{c2})} = 36$–44 nm, where Φ_0 is the magnetic flux quantum. Using the information of $\mu_0 H_{c1} < 5$ mT, the penetration depth λ and the Ginzburg-Landau parameter $\kappa = \lambda/\xi_{GL}$ are evaluated to be $\lambda > 240$ nm and $\kappa > 5.4$ by solving the equation $\mu_0 H_{c1} = (\ln\kappa)\Phi_0/(4\pi\lambda^2)$ [39].

Finally, we show the temperature dependence of the electronic specific heat $C_e(T)$ in Fig. 5(a). We observed a broad but pronounced anomaly starting at 1.5 K, evidencing bulk superconductivity of CaSb$_2$. This broadening is most likely due to inhomogeneous sample property as reflected in the AC susceptibility in Fig. 3.

We fitted the data under zero field assuming that T_c has a spacial distribution described by the lognormal (LN) distribution $f_{LN}(x)$:

$$C_P(T) = C_e(T) + \beta T^3 + \alpha T^5 + A/T^2, \quad (1)$$

$$\frac{C_e(T)}{\gamma T} = 1 + \int_0^{T_o}\left[\frac{C_{BCS}(T;T_c)}{T} - 1\right]f_{LN}(T_o - T_c)dT_c, \quad (2)$$

$$f_{LN}(x) = \frac{1}{\sqrt{2\pi}\sigma x}\exp\left(-\frac{(\ln x - \mu)^2}{2\sigma^2}\right), \quad (3)$$

where $C_P(T)$ is the specific heat including the phononic contribution $\beta T^3 + \alpha T^5$ and the Schottky specific heat A/T^2, and $C_{BCS}(T;T_c)$ is the theoretical specific heat of a fully gapped superconductor derived from the Bardeen-Cooper-Schrieffer (BCS) theory with a critical temperature of T_c [39]. The Schottky specific heat likely originates from the quadrupole splitting of the Sb nucleus or from the Zeeman splitting of the electronic spin of possible impurities. For C_P under 20 mT, we also used $C_{BCS}(T;T_c)$ valid for $H = 0$. The Sommerfeld coefficient and the phononic specific-heat coefficients were determined to be $\gamma = 2.044(3)$ mJ mol^{-1}K^{-2}, $\beta = 0.537(2)$ mJ mol^{-1}K^{-4}, and $\alpha = 0.0037(2)$ mJ mol^{-1}K^{-6} from the data under $\mu_0 H = 80$ mT using Eq. (1) with $C_e = \gamma T$. From γ and β, we evaluated the electronic density of states per spin at the Fermi energy to be $D(E_F) = 0.4336(7)$ eV^{-1} per formula unit and the Debye temperature to be $\Theta_D = 221.5(2)$ K.

From the entropy balance, the thermodynamic T_c was determined to be $T_c = 1.2$ K under 0 mT and $T_c = 1.1$ K
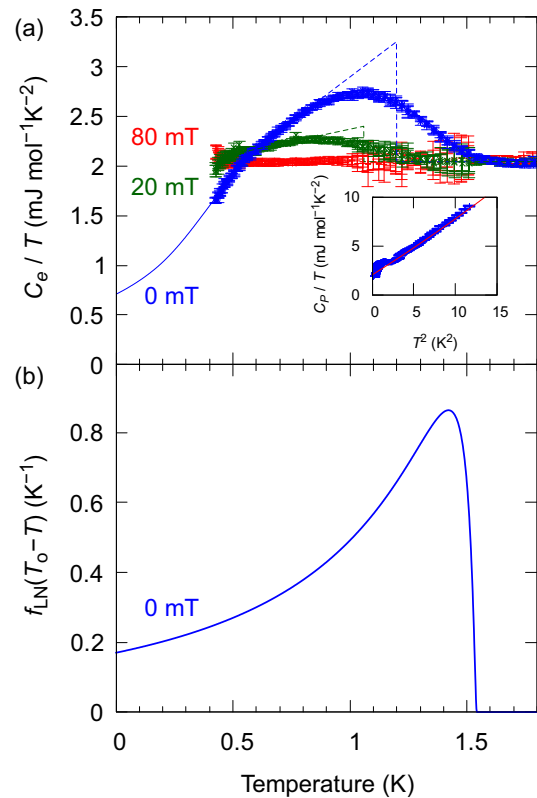

FIG. 5. (a) Temperature dependence of the electronic specific heat divided by temperature, evidencing the bulk superconductivity. The solid curve presents the fitting with the BCS theory with a spatial distribution of the critical temperature. The volume fraction is estimated to be 65%. The dashed lines demonstrate the estimation of the thermodynamic T_c by entropy balance. The inset shows the total specific heat under 0 mT including the phononic and Schottky contributions divided by temperature plotted against T^2. The solid line indicates the electronic and phononic contributions $\gamma + \beta T^2 + \alpha T^4$ extracted from the data under 80 mT. (b) The volume-fraction density $f_{LN}(T_o - T)$ as a function of temperature. Starting from $T_o = 1.54$ K, the largest population exhibits superconductivity at $T_{mode} = 1.42$ K and half of the superconductive part becomes superconducting at $T_{med} = 1.07$ K.

under 20 mT. First, we extrapolated the almost linear part of the experimental data to higher temperature by using a linear fitting. The fitting range was determined so that the root mean square of the residuals becomes the smallest. Then, we defined the thermodynamic T_c as the temperature where the entropies of the extrapolation line and experimental data balance. As we can see in Fig. 4(b), the thermodynamic T_c is almost equal to the temperature at which the resistivity drops to 5% of that in the normal state.

Figure 5(b) presents the temperature dependence of the resultant volume-fraction density $f_{LN}(T_o - T)$. From the fitting, we obtained the onset temperature $T_o = 1.542(8)$ K under zero field. This probability distribution, restricted to $0 \leqslant T \leqslant T_o$, has a mode of $T_{mode} = 1.42$ K and a median of $T_{med} = 1.07$ K. We can see that T_{med} coincides with the temperature at which C_e/T is maximum. Moreover, T_o and T_{mode} roughly correspond to T_c's determined from resistivity using

the 95% and 50% criteria, respectively. The superconducting volume fraction $\int_T^{T_o} f_{LN}(T_o - T_c)dT_c$ is estimated to be 55% at $T = 0.5$ K and 65% at $T = 0$ K. Here, we assume that the entire part of the residual C_e/T of 35% originates from the normal state, namely as a result of the superconducting volume fraction smaller than 100%. This evidences the bulk superconductivity in $CaSb_2$.

IV. DISCUSSION

The first-principles calculation shows that $CaSb_2$ hosts two sets of Fermi surfaces near the zone center (attributable mainly to Sb2) and the zone boundary (Sb1) with almost the same carrier density [31]. Interestingly, the Fermi surface near the zone boundary consists of a pair of concentric cylinders. These cylinders along the AZ line (parallel to the c axis) emerge from a symmetry-protected nodal line after it is slightly self-doped with electrons. Since the nonsymmorphic space group $P2_1/m$ forces an additional orbital degeneracy in addition to the Kramers spin degeneracy, this nodal line near the bottom of the band is fourfold degenerate [31].

Due to such quartet degeneracy, the Fermi surface consists of a pair of cylinders and exhibits a strong mixing among orbitals and spins. Thus, in a similar manner to doped topological insulators [7] and doped Dirac semimetals [13,15], topological superconductivity is naturally expected if the interorbital pairing interaction is dominant. In fact, the zigzag chains consisting of two Sb1 sites in the unit cell may host such interorbital Cooper pairing on each cylinder. If the interorbital pairing involving intersite Cooper pairs is realized, an odd-parity state with nodal lines protected by the nonsymmorphic symmetry at the Brillouin-zone boundary is expected [40]. Even for the intraorbital pairing, an odd-parity state is possible besides even-parity states, but they would be fully gapped.

Another interesting possibility is a time-reversal-breaking chiral p-wave superconductivity [24]. Whereas the present system has a cylindrical Fermi surface not a torus one discussed in Ref. [24], and the relevant space group symmetry is different, it has the same feature that the Fermi surface originates from a nodal line. Therefore, the mechanism for chiral p-wave superconductivity in Ref. [24] might work as well.

Experimental evidence for the nodal structure of the superconducting state will be given by the temperature dependence of the specific heat much below T_c. However, the present data with a broad transition is insufficient for determination of the gap structure. When analyzing the experimental data, we used for simplicity a theoretical curve for a fully gapped superconductivity, which includes some of the p-wave superconducting states such as the Balian-Werthamer (BW) state as well as the s-wave states. Determination of the superconducting gap structure using samples with a sharp transition is a challenge of future work.

V. CONCLUSION

We report the discovery of superconductivity in $CaSb_2$, which has nodal lines in the bulk electronic band structure crossing the Fermi energy, protected by a nonsymmorphic crystalline symmetry. Both DC magnetization and specific heat indicate the bulk superconductivity. The transition temperature is determined to be 1.7 K from magnetic susceptibility and resistivity. The lower critical field is smaller than 5 mT, and the upper critical field is estimated to be 0.17–0.26 T. From these critical fields, the Ginzburg-Landau parameter is evaluated to be $\kappa > 5.4$. We hope this work stimulates further investigations of the superconductivity in nonsymmorphic Dirac-line materials.

[1] M. Z. Hasan and C. L. Kane, Colloquium: Topological insulators, Rev. Mod. Phys. **82**, 3045 (2010).

[2] X.-L. Qi and S.-C. Zhang, Topological insulators and superconductors, Rev. Mod. Phys. **83**, 1057 (2011).

[3] Y. Ando, Topological insulator materials, J. Phys. Soc. Jpn. **82**, 102001 (2013).

[4] Y. Tanaka, M. Sato, and N. Nagaosa, Symmetry and topology in superconductors–odd-frequency pairing and edge states, J. Phys. Soc. Jpn. **81**, 011013 (2012).

[5] M. Sato and S. Fujimoto, Majorana fermions and topology in superconductors, J. Phys. Soc. Jpn. **85**, 072001 (2016).

[6] M. Sato and Y. Ando, Topological superconductors: a review, Rep. Prog. Phys. **80**, 076501 (2017).

[7] L. Fu and E. Berg, Odd-Parity Topological Superconductors: Theory and Application to $Cu_xBi_2Se_3$, Phys. Rev. Lett. **105**, 097001 (2010).

[8] S. Sasaki, M. Kriener, K. Segawa, K. Yada, Y. Tanaka, M. Sato, and Y. Ando, Topological Superconductivity in $Cu_xBi_2Se_3$, Phys. Rev. Lett. **107**, 217001 (2011).

[9] K. Matano, M. Kriener, K. Segawa, Y. Ando, and G.-q. Zheng, Spin-rotation symmetry breaking in the superconducting state of $Cu_xBi_2Se_3$, Nat. Phys. **12**, 852 (2016).

[10] S. Yonezawa, K. Tajiri, S. Nakata, Y. Nagai, Z. Wang, K. Segawa, Y. Ando, and Y. Maeno, Thermodynamic evidence for nematic superconductivity in $Cu_xBi_2Se_3$, Nat. Phys. **13**, 123 (2017).

[11] B. Yan and C. Felser, Topological materials: Weyl semimetals, Annu. Rev. Condens. Matter. Phys. **8**, 337 (2017).

[12] N. P. Armitage, E. J. Mele, and A. Vishwanath, Weyl and Dirac semimetals in three-dimensional solids, Rev. Mod. Phys. **90**, 015001 (2018).

[13] S. Kobayashi and M. Sato, Topological Superconductivity in Dirac Semimetals, Phys. Rev. Lett. **115**, 187001 (2015).

[14] Y. Li and F. D. M. Haldane, Topological Nodal Cooper Pairing in Doped Weyl Metals, Phys. Rev. Lett. **120**, 067003 (2018).

[15] T. Kawakami, T. Okamura, S. Kobayashi, and M. Sato, Topological Crystalline Materials of $J = 3/2$ Electrons: Antiperovskites, Dirac Points, and High Winding Topological Superconductivity, Phys. Rev. X **8**, 041026 (2018).

[16] L. He, Y. Jia, S. Zhang, X. Hong, C. Jin, and S. Li, Pressure-induced superconductivity in the three-dimensional topological Dirac semimetal Cd_3As_2, npj Quantum Mater. **1**, 16014 (2016).

[17] M. Oudah, A. Ikeda, J. N. Hausmann, S. Yonezawa, T. Fukumoto, S. Kobayashi, M. Sato, and Y. Maeno, Superconductivity in the antiperovskite Dirac-metal oxide $Sr_{3-x}SnO$, Nat. Commun. **7**, 13617 (2016).

[18] C. Fang, Y. Chen, H.-Y. Kee, and L. Fu, Topological nodal line semimetals with and without spin-orbital coupling, Phys. Rev. B **92**, 081201(R) (2015).

[19] A. Yamakage, Y. Yamakawa, Y. Tanaka, and Y. Okamoto, Line-node Dirac semimetal and topological insulating phase in noncentrosymmetric pnictides $CaAgX$ ($X =$ P, As), J. Phys. Soc. Jpn. **85**, 013708 (2016).

[20] S. Kobayashi, Y. Yamakawa, A. Yamakage, T. Inohara, Y. Okamoto, and Y. Tanaka, Crossing-line-node semimetals: General theory and application to rare-earth trihydrides, Phys. Rev. B **95**, 245208 (2017).

[21] Y. Huh, E.-G. Moon, and Y. B. Kim, Long-range Coulomb interaction in nodal-ring semimetals, Phys. Rev. B **93**, 035138 (2016).

[22] M. Hirayama, R. Okugawa, T. Miyake, and S. Murakami, Topological Dirac nodal lines and surface charges in fcc alkaline earth metals, Nat. Commun. **8**, 14022 (2017).

[23] S. T. Ramamurthy and T. L. Hughes, Quasitopological electromagnetic response of line-node semimetals, Phys. Rev. B **95**, 075138 (2017).

[24] H. Shapourian, Y. Wang, and S. Ryu, Topological crystalline superconductivity and second-order topological superconductivity in nodal-loop materials, Phys. Rev. B **97**, 094508 (2018).

[25] M. N. Ali, Q. D. Gibson, T. Klimczuk, and R. J. Cava, Non-centrosymmetric superconductor with a bulk three-dimensional Dirac cone gapped by strong spin-orbit coupling, Phys. Rev. B **89**, 020505(R) (2014).

[26] J.-M. Carter, V. V. Shankar, M. A. Zeb, and H.-Y. Kee, Semimetal and topological insulator in perovskite iridates, Phys. Rev. B **85**, 115105 (2012).

[27] Y. Chen, Y.-M. Lu, and H.-Y. Kee, Topological crystalline metal in orthorhombic perovskite iridates, Nat. Commun. **6**, 6593 (2015).

[28] Q.-F. Liang, J. Zhou, R. Yu, Z. Wang, and H. Weng, Node-surface and node-line fermions from nonsymmorphic lattice symmetries, Phys. Rev. B **93**, 085427 (2016).

[29] Y. Sun, Y. Zhang, C.-X. Liu, C. Felser, and B. Yan, Dirac nodal lines and induced spin Hall effect in metallic rutile oxides, Phys. Rev. B **95**, 235104 (2017).

[30] J. J. Neumeier and M. G. Smith, Superconductivity in quasi-one-dimensional $BaNbS_3$, Physica C **542**, 1 (2017).

[31] K. Funada, A. Yamakage, N. Yamashina, and H. Kageyama, Spin-orbit-coupling-induced type-I/type-II Dirac nodal-line metal in nonsymmorphic $CaSb_2$, J. Phys. Soc. Jpn. **88**, 044711 (2019).

[32] K. Deller and B. Eisenmann, Darstellung und Kristallstruktur von $CaSb_2$, Z. Anorg. Allg. Chem. **425**, 104 (1976).

[33] K. Momma and F. Izumi, VESTA 3 for three-dimensional visualization of crystal, volumetric and morphology data, J. Appl. Crystallogr. **44**, 1272 (2011).

[34] H. Okamoto, Ca-Sb (Calcium-Antimony), J. Phase Equilibria **18**, 313 (1997).

[35] S. Yonezawa, T. Higuchi, Y. Sugimoto, C. Sow, and Y. Maeno, Compact AC susceptometer for fast sample characterization down to 0.1 K, Rev. Sci. Instrum. **86**, 093903 (2015).

[36] A. Aharoni, Demagnetizing factors for rectangular ferromagnetic prisms, J. Appl. Phys. **83**, 3432 (1998).

[37] M. Yang, Y. H. Kao, Y. Xin, and K. W. Wong, Chemical doping and intergranular magnetic-field effects in bulk thallium-based superconductors, Phys. Rev. B **50**, 13653 (1994).

[38] S. Kittaka, T. Nakamura, H. Yaguchi, S. Yonezawa, and Y. Maeno, Spatial development of superconductivity in the Sr_2RuO_4-Ru eutectic system, J. Phys. Soc. Jpn. **78**, 064703 (2009).

[39] M. Tinkham, *Introduction to Superconductivity* (Dover Publications, New York, 2004).

[40] S. Kobayashi, Y. Yanase, and M. Sato, Topologically stable gapless phases in nonsymmorphic superconductors, Phys. Rev. B **94**, 134512 (2016).